

## THE ASYMMETRIC NEBULA SURROUNDING THE EXTREME RED SUPERGIANT VY CANIS MAJORIS<sup>1</sup>

NATHAN SMITH, ROBERTA M. HUMPHREYS, KRIS DAVIDSON, ROBERT D. GEHRZ,<sup>2</sup> AND M. T. SCHUSTER

Department of Astronomy, University of Minnesota, 116 Church Street, SE, Minneapolis, MN 55455; nathans@astro.umn.edu; roberta@isis.spa.umn.edu

AND

JOACHIM KRAUTTER<sup>2</sup>

Landessternwarte Königstuhl, D-69117 Heidelberg, Germany

Received 2000 August 1; accepted 2000 November 13

### ABSTRACT

We present *HST*/WFPC2 images plus ground-based infrared images and photometry of the very luminous OH/IR star VY Canis Majoris. Our WFPC2 data show a complex distribution of knots and filamentary arcs in the asymmetric reflection nebula around the obscured central star. The reflection arcs may result from multiple, asymmetric ejection episodes due to localized events on VY CMA's surface. Such events probably involve magnetic fields and convection, by analogy with solar activity. Surface photometry indicates that the star may have experienced enhanced mass loss over the past 1000 yr. We also demonstrate that the apparent asymmetry of the nebula results from a combination of high extinction and backscattering by dust grains. Thermal-infrared images reveal a more symmetric distribution, elongated along a nearly east-west direction. VY CMA probably has a flattened disklike distribution of dust with a northeast-southwest polar axis and may be experiencing activity analogous to solar prominences. The presence of an axis of symmetry raises interesting questions for a star the size of Saturn's orbit. Magnetic fields and surface activity may play an important role in VY CMA's mass-loss history.

*Key words:* circumstellar matter — stars: individual (VY Canis Majoris) — supergiants

### 1. INTRODUCTION

The powerful infrared source VY Canis Majoris (M5e Ia) is one of the most luminous known red supergiants. At a distance of 1.5 kpc (Herbig 1972; Lada & Reid 1978; Marvel 1997), VY CMA has a luminosity of about  $5 \times 10^5 L_{\odot}$ , near the empirical upper luminosity limit for evolved cool stars (see Humphreys & Davidson 1994). It belongs to the class of very luminous evolved stars called cool hypergiants (see review by de Jager 1998). This brief evolutionary stage is characterized by high mass loss. VY CMA's very high mass-loss rate ( $2$  to  $4 \times 10^{-4} M_{\odot} \text{ yr}^{-1}$ ; Danchi et al. 1994) fuels its optically thick circumstellar envelope and its powerful infrared (IR) excess radiation.

VY CMA has an asymmetric red reflection nebula several arcseconds across, easily visible even in small telescopes (e.g., Perrine 1923). Early visual observations produced a confused picture, with reports of knots that come and go (See 1897; Perrine 1923; van den Bos 1927; Herbig 1972 summarized the early observations). With these apparent “companions,” VY CMA was considered a multiple system and was included in catalogs of binary stars (e.g., as ADS 6033AB). Modern measurements by Worley (1972) showed that it is instead a single source with a complex nebular structure, and Herbig (1972) confirmed that its

“companions” were dusty condensations that produce strong and variable polarization (Serkowski 1969a, 1969b; Hashimoto et al. 1970; Forbes 1971). Recent near-IR images by Monnier et al. (1999) resolve some of the circumstellar dust condensations within a few arcseconds of the star and show that the asymmetry of the nebula extends to IR wavelengths.

Ever since the discovery of its strong OH, H<sub>2</sub>O, and SiO maser emission (Wilson & Barrett 1968; Eliasson & Bartlett 1969; Snyder & Buhl 1975), VY CMA has been extensively observed at millimeter wavelengths. Its 1612 MHz OH maser emission is variable (e.g., Rosen et al. 1978; Zheng, Scalise, & Han 1998) and shows the double-peaked velocity structure characteristic of an expanding shell. Interferometric maps reveal complex structure that may be either an expanding disk or a bipolar outflow (Bowers, Johnston, & Spencer 1983), while the H<sub>2</sub>O masers show proper motions indicating outflow (Richards, Yates, & Cohen 1998). The OH and H<sub>2</sub>O masers indicate expansion velocities of  $\sim 30$  to  $40 \text{ km s}^{-1}$ , and we adopt  $v_{\text{exp}} = 35 \text{ km s}^{-1}$  throughout this paper. Optical and IR observations (Herbig 1972; McCarthy 1979) also provide evidence for a disklike geometry near the central object. Wittkowski, Langer, & Weigelt (1998) identify an extended circumstellar envelope, elongated by 0'.2 in a north-south direction in their diffraction-limited speckle images at wavelengths of 0.8 to 2  $\mu\text{m}$ . Near-IR aperture-masked interferometry by Monnier et al. (1999) reveals a southward extension of circumstellar emission within 0'.1 of the star, but no clear disklike or bipolar geometry is obvious in the images.

We are using images and spectroscopy from the *Hubble Space Telescope* (*HST*) in combination with ground-based IR images and spectra to trace the mass-loss histories and

<sup>1</sup> Based on observations made with the NASA/ESA *Hubble Space Telescope*, obtained at the Space Telescope Science Institute, which is operated by the Association of Universities for Research in Astronomy, Inc., under NASA contract NAS 5-26555.

<sup>2</sup> Contributions by these authors include observations collected at the European Southern Observatory, La Silla, Chile under programs 57.C-0719 and 62.I-0477.

TABLE 1  
HST/WFPC2 OBSERVATIONS<sup>a</sup>

Filter	$\lambda$ (Å)	$\Delta\lambda$ (Å)	Exp. Times (s)
F410M .....	4090.1	146.7	5, 16, 2 × 60
F547M .....	5476.3	483.1	0.11, 0.5, 2, 5, 16
F656N .....	6563.7	21.4	0.4, 2, 14, 2 × 30
F1042M .....	10183.5	365.0	0.11, 0.5, 3, 2 × 7

<sup>a</sup> Obtained 1999 March 22.

TABLE 2  
IR IMAGING OBSERVATIONS (ESO 3.6 M)

Filter	$\lambda$ ( $\mu\text{m}$ )	$\Delta\lambda$ ( $\mu\text{m}$ )	Instrument	Date
J .....	1.25	0.30	ADONIS/SHARPII+	1999 Mar 11
H .....	1.64	0.35	ADONIS/SHARPII+	1999 Mar 11
H <sub>2</sub> .....	2.121	0.015	ADONIS/SHARPII+	1999 Mar 11
H <sub>2</sub> cont .....	2.145	0.017	ADONIS/SHARPII+	1999 Mar 11
M .....	4.7	0.99	TIMMI	1996 Apr 05
N1 .....	8.4	0.96	TIMMI	1996 Apr 05
N2 .....	9.7	1.29	TIMMI	1996 Apr 05

final evolutionary stages of selected cool hypergiants. With its strong masering, high mass-loss rate, and circumstellar nebula, VY CMa is one of our primary targets. The first *HST* images of VY CMa, obtained by Kastner & Weintraub (1998) with the Faint Object Camera (FOC), showed the obscured central object and the brightest inner nebulosity. We have subsequently obtained images at different wavelengths using the Wide Field Planetary Camera 2

(WFPC2), using a range of exposure times with each filter to cover the wide dynamic range of the bright central object and its faint outer nebulosity. In this paper we describe these new *HST* images, as well as ground-based IR images and photometry of VY CMa. They reveal a complex circumstellar environment with large arcs that are evidence for

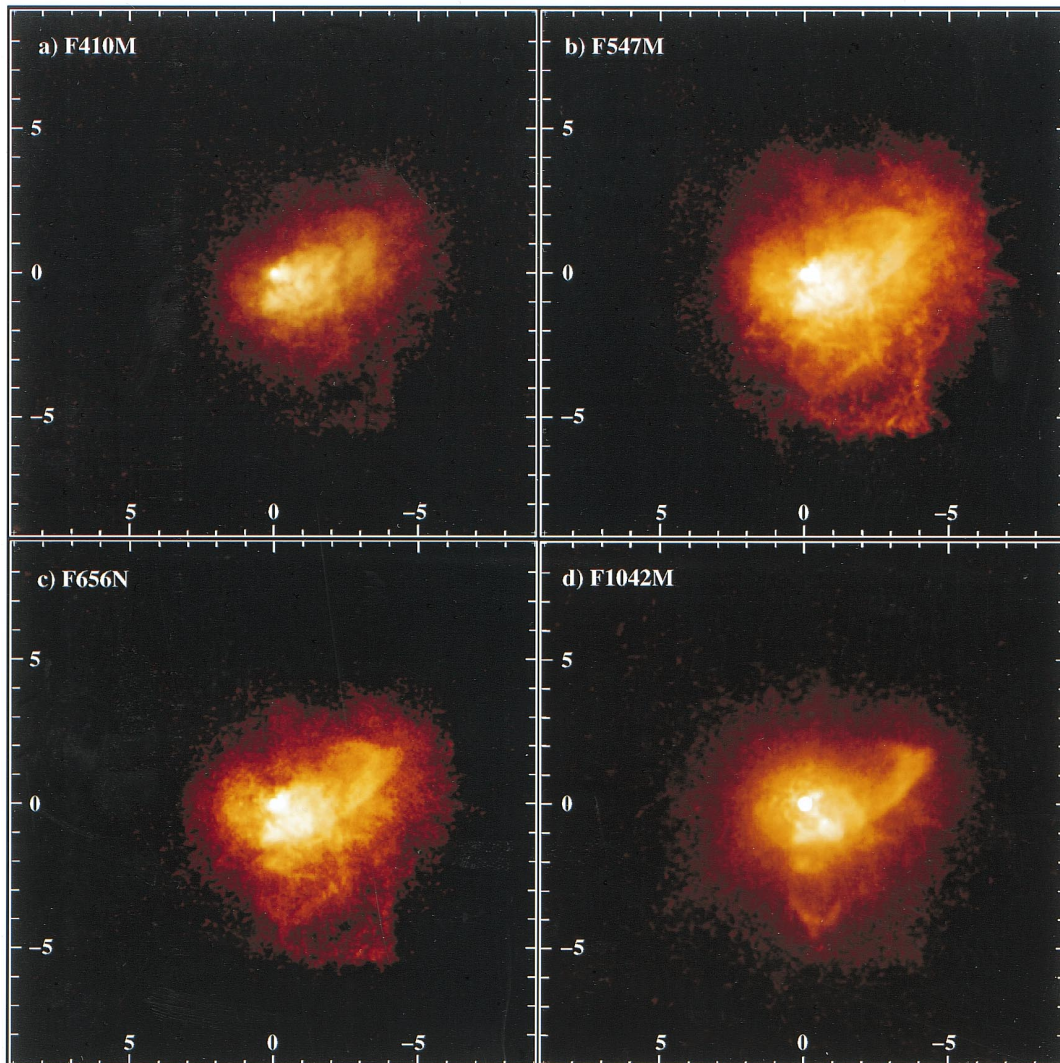


FIG. 1.—*HST*/WFPC2 images of VY CMa in four filters (a) F410M, (b) F547M, (c) F656N, and (d) F1042M (see Table 1). Horizontal and vertical axes denote right ascension and declination offsets in arcseconds from the position of the central star in the F656N and F1042M filters. Images are displayed with a logarithmic stretch from (a)  $10^{-20}$  to  $10^{-15}$ , (b)  $10^{-23.3}$  to  $10^{-15}$ , and (c)  $10^{-22}$  to  $10^{-15}$ , and (d)  $10^{-21}$  to  $10^{-14}$  ergs  $\text{s}^{-1} \text{cm}^{-2} \text{Å}^{-1}$ .

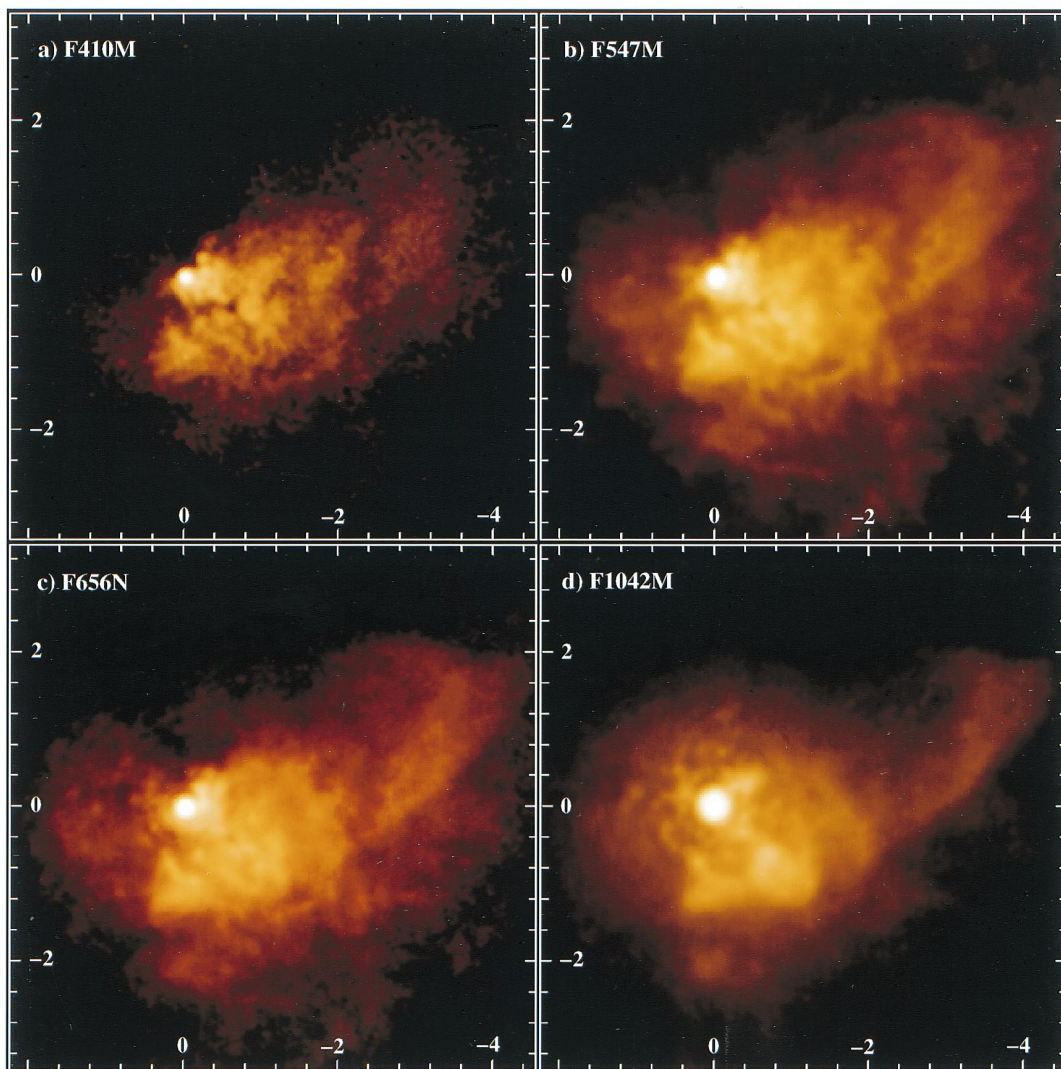


FIG. 2.—Same as Fig. 1, but with a greater dynamic range and smaller field of view detailing the brightest structures close to the star

multiple asymmetric ejections, plus a smaller elongated structure visible only at mid-IR wavelengths.

## 2. MULTIWAVELENGTH IMAGING

### 2.1. *HST*/WFPC2 Images

We observed VY CMA with the WFPC2 on 1999 March 22. The object was positioned on the Planetary Camera chip, with a pixel scale of  $0''.0455$ . We used the F410M, F547M, and F1042M medium-width continuum filters, and the narrow  $H\alpha$  filter (F656N) with multiple exposures to detect the faint circumstellar nebulosity and to avoid saturation from the bright central star (see Table 1).

The longer exposures were combined to remove cosmic-ray hits, and distortions were corrected using the CRREJ and DRIZZLE tasks in IRAF/STSDAS. Remaining cosmic rays were removed by interpolating over adjacent pixels. Saturated pixels from the bright central star were patched over with corresponding data from shorter exposures. A more detailed description of our procedure can be found in the discussion of the *HST*/WFPC2 images of IRC + 10420 (Humphreys et al. 1997). To suppress the prominent diffraction spikes and annular rings in the *HST* point-spread func-

tion (PSF), we deconvolved the raw images with the LUCY task provided in IRAF/STSDAS using an artificial TinyTim PSF constructed for each filter (see the *HST* Data Handbook). Only five to 10 iterations were used, and the resulting images are shown in Figures 1 and 2. Figure 3 shows a composite three-color image of the relative spatial distribution of flux in each filter, with the color scheme described in the figure caption.

### 2.2. Infrared images

Near-IR images of VY CMA were obtained on 1999 March 11 with the ADONIS/SHARPII+ adaptive optics and near-IR camera system mounted on the ESO 3.6 m telescope at LaSilla, Chile. SHARPII+ has a  $256 \times 256$  NICMOS3 array, which we used with a pixel scale of  $0''.055$ . These and the mid-IR imaging observations described below are summarized in Table 2. VY CMA was imaged in the *J* and *H* continuum filters, as well as the  $2.14 \mu\text{m}$  continuum and  $2.122 \mu\text{m}$   $\text{H}_2$  1–0 S(1) narrowband filters. The observations are similar in many respects to the near-IR ADONIS images obtained by Monnier et al. (1999) using the same telescope, except that these have a larger field-of-view and include additional filters. We observed HR 4023



FIG. 3.—Composite color *HST* image of VY CMA with the F410M filter in blue, F547M in green, and a combination of the F656N and F1042M filters in red. (*a*, top panel) shows the full nebula (see Fig. 1), and (*b*, lower panel) shows detailed structure within a few arcseconds of the star (see Fig. 2).

immediately after VY CMA to calibrate the images and to define the PSF of the observations. Individual frames were combined by standard shift-and-add routines. The near-IR images of VY CMA were deconvolved with 15 to 20 iterations of LUCY task in IRAF/STSDAS, using HR 4023 as the PSF. Resulting images are shown in Figure 4, which have peak-to-noise dynamic ranges between  $8 \times 10^4$  ( $2.14 \mu\text{m}$ ) and  $1.6 \times 10^5$  ( $1.25 \mu\text{m}$ ). Many low-level background structures, such as the vertical striping and diffraction spikes, are residual detector artifacts that were present before deconvolution.

We also obtained mid-IR images to search for extended warm circumstellar dust. These observations were made on 1996 April 5 UT with the Thermal Infrared Multi-Mode Instrument (TIMMI) mounted at the Cassegrain focus of

the ESO 3.6 m telescope at LaSilla, Chile. With this instrument configuration, TIMMI's  $64 \times 64$  pixel Ga:Si array has a pixel scale of  $0''.336$ . Images were obtained at wavelengths of 4.7, 8.4, and  $9.8 \mu\text{m}$ , corresponding to the M, N1, and N2 filters in the TIMMI filter set (see Table 2). They were calibrated with the IR standard star  $\gamma$  Cru. Background removal and flat fielding was accomplished with a chopping secondary mirror using the standard IR beam-switching technique described by Gehrz & Ney (1992), with  $30''$  between the centers of the source and reference images. Individual frames in each filter were then combined by shifting and adding to produce the final mid-IR images of VY CMA and  $\gamma$  Cru. To investigate extended structure around VY CMA, we subtracted a normalized PSF defined by the images of  $\gamma$  Cru. The PSF and VY CMA images were registered by aligning the emission peaks. The resulting PSF-subtracted images at 4.7, 8.4, and  $9.7 \mu\text{m}$  are shown in Figure 5. All show emission that is elongated along a nearly east-west direction. Several other targets were observed the same night as VY CMA, and none showed a similar east-west elongation (e.g., Smith, Gehrz, & Krautter 1998; Gehrz et al. 1999).

### 3. PHOTOMETRY AND THE SPECTRAL ENERGY DISTRIBUTION

Figures 6*a* and 6*b* show photometry based on the optical and near-IR images, using a range of circular synthetic apertures centered on the star. The near-IR photometry was measured in the raw (nondeconvolved) images. Fluxes in the smallest diameters (essentially the central star) and the largest are given in Table 3. We also measured fluxes within a  $10''$  diameter in the mid-IR images, and the fluxes of the normalized PSF's used for subtraction. This photometry is included in Table 3 as “total” and “star,” respectively.

We also measured standard broadband IR photometry on 2000 January 5 UT with the University of Minnesota Ga:Ge multifilter bolometer at the Cassegrain focus of the 1.5 m UM/UCSD Mount Lemmon Observing Facility (MLOF). The calibration of the MLOF photometric system is described by Ney (1974). The  $9''.33$  aperture includes emis-

TABLE 3  
IMAGING PHOTOMETRY<sup>a</sup>

$\lambda$ ( $\mu\text{m}$ )	$F_{\lambda}(\text{star})^b$	$F_{\lambda}(\text{total})^c$
0.41.....	$1.95 \times 10^{-17}$	$2.24 \times 10^{-16}$
0.55.....	$6.65 \times 10^{-16}$	$2.18 \times 10^{-15}$
0.66.....	$2.85 \times 10^{-15}$	$6.50 \times 10^{-15}$
1.02.....	$6.10 \times 10^{-15}$	$1.39 \times 10^{-14}$
1.25.....	$1.36 \times 10^{-14}$	$2.01 \times 10^{-14}$
1.65.....	$1.88 \times 10^{-14}$	$2.37 \times 10^{-14}$
2.12.....	$2.85 \times 10^{-14}$	$3.31 \times 10^{-14}$
2.14.....	$2.42 \times 10^{-14}$	$3.20 \times 10^{-14}$
4.7.....	$5.79 \times 10^{-14}$	$6.26 \times 10^{-14}$
8.4.....	$3.01 \times 10^{-14}$	$3.90 \times 10^{-14}$
9.8.....	$1.88 \times 10^{-14}$	$3.31 \times 10^{-14}$

<sup>a</sup> Fluxes are given in  $\text{W cm}^{-2} \mu\text{m}^{-1}$ .

<sup>b</sup>  $0''.22$  diameter aperture at 0.41 to  $1.02 \mu\text{m}$ ,  $0''.4$  diameter aperture at 1.25 to  $2.14 \mu\text{m}$ , and 4.7 to  $9.8 \mu\text{m}$  fluxes correspond to a subtracted PSF (see text).

<sup>c</sup>  $14''.6$  diameter aperture at 0.41 to  $1.02 \mu\text{m}$ ,  $11''$  diameter aperture at 1.25 to  $2.14 \mu\text{m}$ , and a  $10''$  aperture at 4.7 to  $9.8 \mu\text{m}$  (PSF-subtracted).

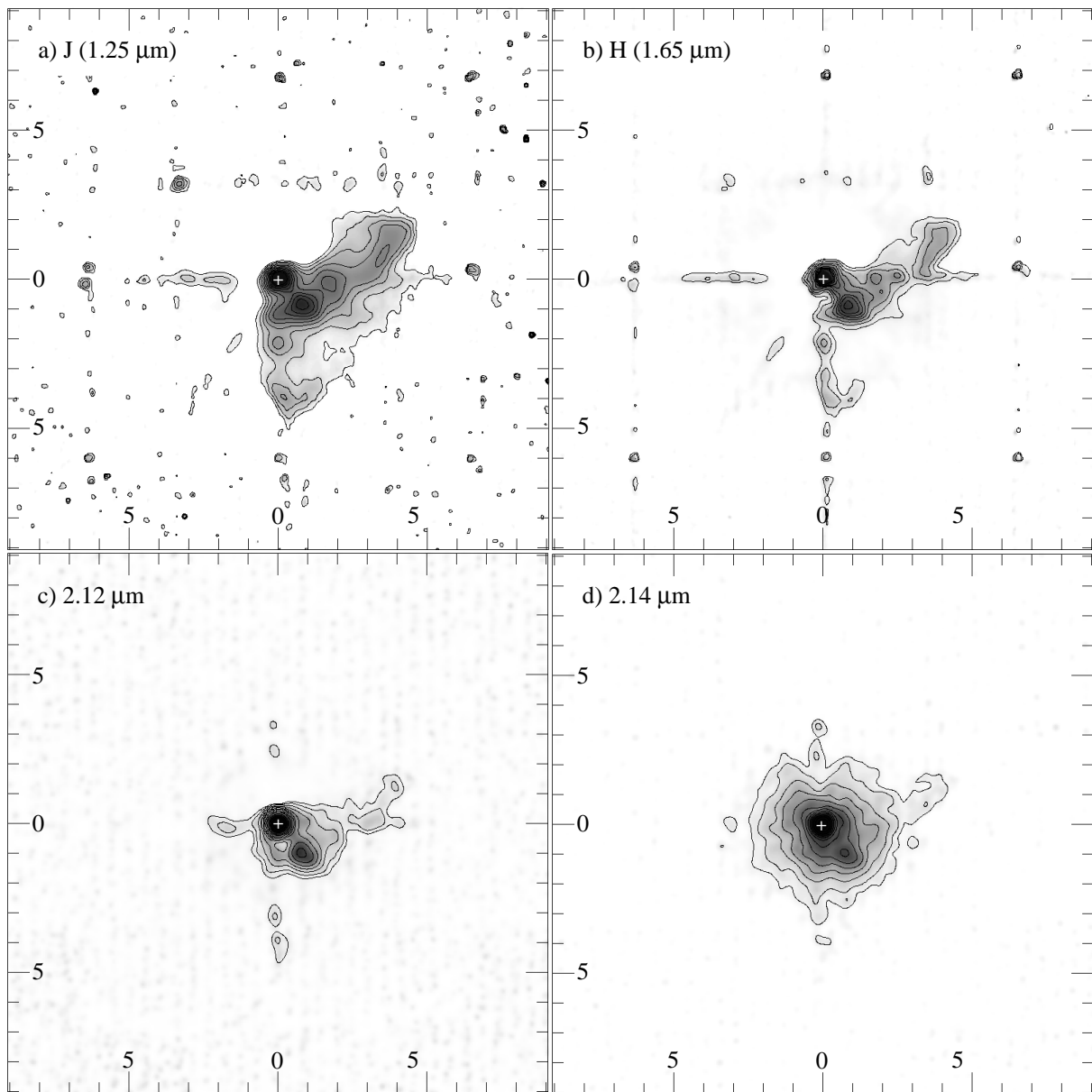


FIG. 4.—Near-IR adaptive optics images of VY CMA obtained with the ESO 3.6 m telescope in 1999 March at (a) 1.25  $\mu\text{m}$ , broadband  $J$ , (b) 1.65  $\mu\text{m}$ , broadband  $H$ , (c) 2.12  $\mu\text{m}$ , and (d) 2.14  $\mu\text{m}$ . Each contour is a factor of 2 above the preceding contour, with the following values for the lowest contour in  $\text{W cm}^{-2} \mu\text{m}^{-1} \text{arcsec}^{-2}$ : (a)  $1.2 \times 10^{-17}$ , and (b, c, d)  $2.4 \times 10^{-17}$ . Horizontal and vertical axes denote right ascension and declination offsets in arcseconds.

sion from the central star and the nebula, and the resulting photometry is summarized in Table 4.

*Large-aperture photometry.*—We combined the large-aperture optical and IR imaging photometry with the broadband MLOF photometry to assess the optical-to-IR spectral energy distribution shown in Figure 7. The various data sets agree well, and VY CMA shows a smooth, broad continuum. The WFPC2 F656N flux appears to exceed the smooth continuum level by  $\sim 2 \times 10^{-17} \text{ W cm}^{-2} \mu\text{m}^{-1}$  (less than  $1 L_{\odot}$  at  $D = 1.5 \text{ kpc}$ ), probably due to emission from  $\text{Ca I } \lambda 6572$  and possibly some  $\text{H}\alpha$  (G. Wallerstein 2000, private communication).  $\text{H}\alpha$  is usually faint in VY CMA, but Wallerstein (1958) noticed variability in this line. There appears to be a depression in the  $K$ -band flux below the expected continuum level. This is probably absorption in the 2.3  $\mu\text{m}$  CO band, characteristic of very luminous cool supergiants and present in the near-IR spectrum of VY

CMA (Low et al. 1970). Figure 7 also shows a flattened 10  $\mu\text{m}$  silicate emission feature and a possible excess at 18  $\mu\text{m}$ , suggesting the presence of silicate grains in an oxygen-rich environment. The flattened shape of the 10  $\mu\text{m}$  silicate emission may indicate a high optical depth or large grains. The 10  $\mu\text{m}$  feature may be variable, since it was present in early IR data (Humphreys, Strecker, & Ney 1972; Gehrz, Ney, & Strecker 1970; Gillett, Stein, & Solomon 1970; Low et al. 1970; Hyland et al. 1969), but not in spectra obtained in 1994 to 1995 by Monnier, Geballe, & Danchi (1998). The total integrated flux from 0.4 to 25  $\mu\text{m}$  is  $6.5 \times 10^{-13} \text{ W cm}^{-2}$ , corresponding to a luminosity of  $4.1 \times 10^5 L_{\odot}$  at a distance of 1.5 kpc, assuming isotropic emission. Longer wavelength fluxes observed with IRAS (Rowan-Robinson et al. 1986) increase this by a few percent.

*The central star.*—The dotted line in Figure 7 represents the approximate contribution of the central emission peak

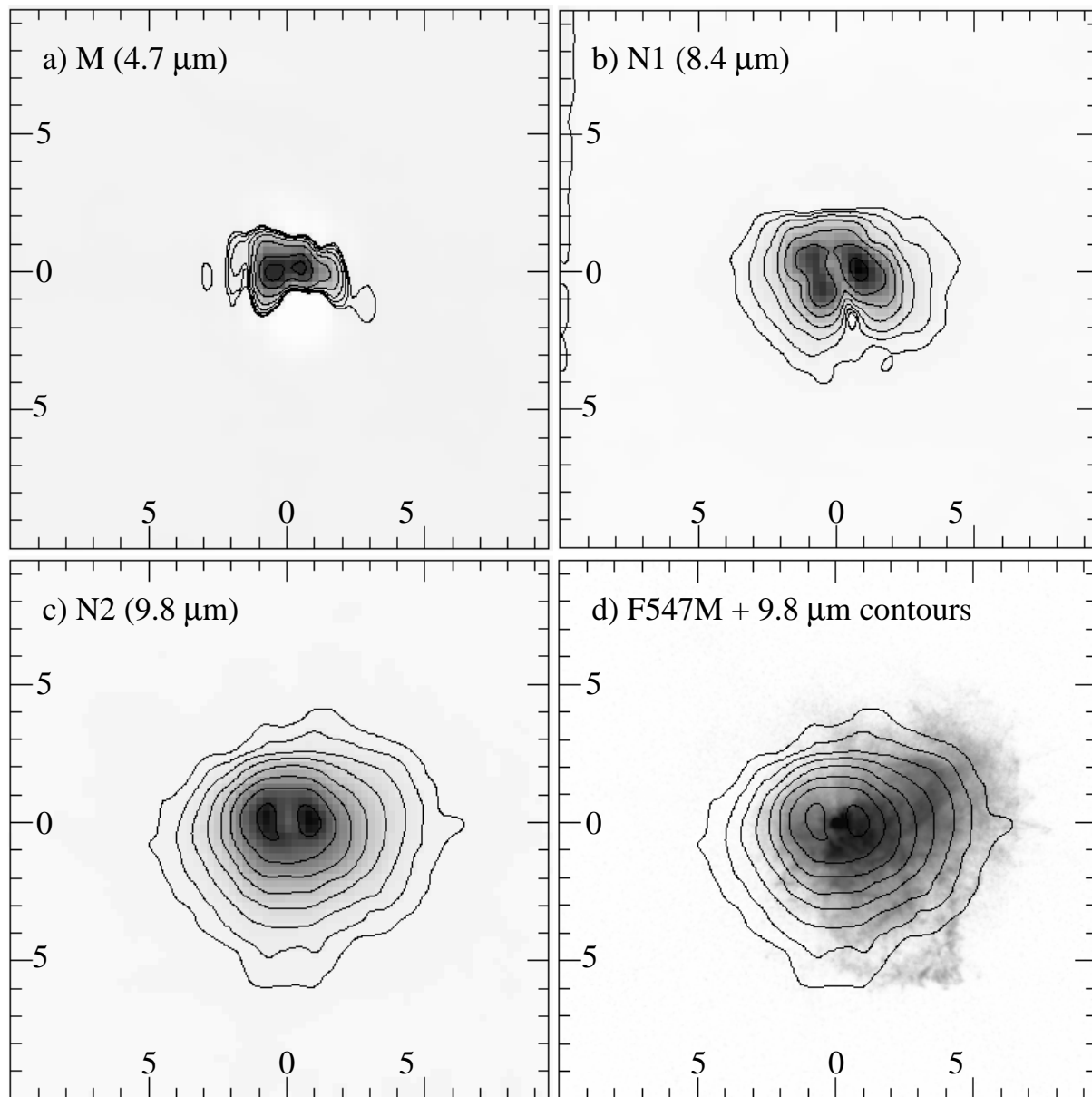


FIG. 5.—Thermal-IR PSF-subtracted images of VY CMa obtained with TIMMI on the ESO 3.6 m telescope in 1996 April at (a) 4.7  $\mu\text{m}$ , (b) 8.4  $\mu\text{m}$ , and (c) 9.8  $\mu\text{m}$ . For each image, a normalized image of the standard star  $\gamma$  Cru has been subtracted. Each contour is a factor of 2 above the preceding contour, with the following values for the lowest contour in  $\text{W cm}^{-2} \mu\text{m}^{-1} \text{arcsec}^{-2}$ : (a)  $2.2 \times 10^{-17}$ , (b)  $2.7 \times 10^{-17}$ , and (c)  $10^{-17}$ . (d) 9.8  $\mu\text{m}$  contours superposed on the F547M *HST*/WFPC2 image. Horizontal and vertical axes denote right ascension and declination offsets in arcseconds.

to the spectral distribution; note that the smallest-diameter aperture is dominated by scattered light at blue wavelengths and represents an upper limit to the flux from the central source at mid-IR wavelengths because of inadequate spatial resolution. The WFPC2 and near-IR continuum measurements reveal a very red object, with a F410M/F547M color of  $\sim 3.8$  mag. The central star also had excess emission in the  $\text{H}\alpha$  filter, as mentioned above for the larger aperture. The central star's  $\lambda F_\lambda$  continues to rise at wavelengths up to about 5  $\mu\text{m}$ .<sup>3</sup> The 2.14  $\mu\text{m}$  flux from the star may be affected by CO absorption, as noted above for the

<sup>3</sup> The discontinuity in the continuum level at  $\lambda \sim 1 \mu\text{m}$  results from the difference in resolution and sampling-aperture size between the *HST* and the ground-based images.

larger aperture. The higher 2.122  $\mu\text{m}$  flux may indicate  $\text{H}_2$  emission, but previous spectra have not shown this emission feature (Low et al. 1970). At wavelengths longer than 3  $\mu\text{m}$ , the central source is probably dominated by thermal emission from hot dust in a compact shell or dense wind around the star (see also § 6.2). The dust forming in this dense stellar wind probably blocks much of the light from the star.

Previous observations suggested appreciable circumstellar extinction. Kastner & Weintraub (1998) noted that the central star's apparent position depends on wavelength, presumably due to a gradient in local extinction and reddening. Our WFPC2 images include a field star that allows us to check this result without relying on absolute pointing as they did with their FOC data. The central peak of VY CMa in our F656N image is indeed located about 25 mas northeast of the peak in the F410M image while the

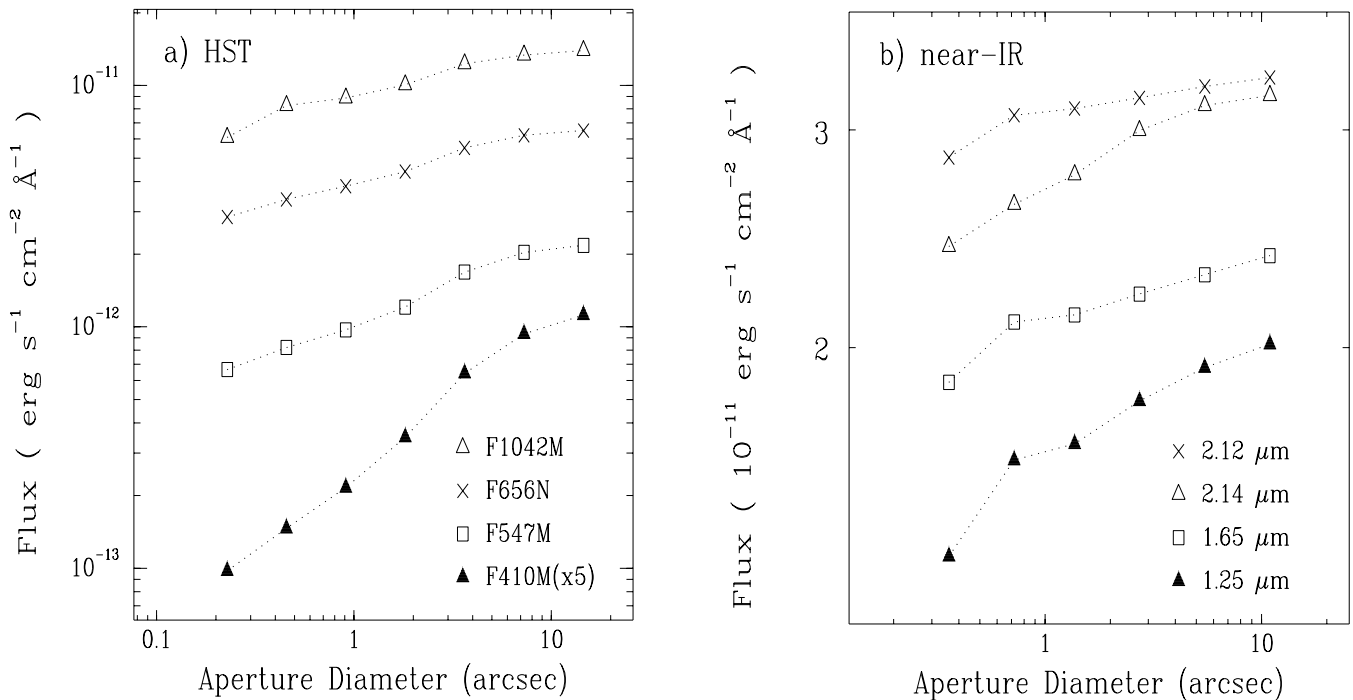


FIG. 6.—Aperture photometry for the *HST*/WFPC2 images (a) and ground-based near-IR images (b) measured with a range of different aperture sizes

F547M position is intermediate; the position angle of the trend is  $20^\circ \pm 10^\circ$ , consistent with Kastner & Weintraub's result.

*Extended emission.*— Contributions to the total observed flux from the extended emission, separated into scattered light and thermal emission, are indicated by the dashed lines in Figure 7. Light scattered by extended circumstellar dust dominates the observed optical flux, especially at short wavelengths. In the F410M filter, the central object contributes less than 10% of the total observed flux, and much of this is due to scattering by dust within 0'.1 of the star, since the peak is not a point source. Scattered light from the nebula is a smaller fraction of the flux at longer wave-

lengths, but still occurs significantly at 1 to 2  $\mu\text{m}$ , suggesting the presence of large grains. Around 2  $\mu\text{m}$ , the observed flux from the nebula is above the dashed line representing the contribution of scattered light in Figure 7, probably because

TABLE 4  
MLOF PHOTOMETRY OF VY CMA

$\lambda$ ( $\mu\text{m}$ )	$\Delta\lambda$ ( $\mu\text{m}$ )	Magnitude	$F_\lambda^a$	$\pm F_\lambda^b$
1.25	0.2	2.895	2.02	0.005
1.65	0.3	1.515	2.77	0.007
2.34	0.5	-0.059	3.58	0.007
3.65	1.2	-2.378	5.75	0.012
4.90	0.7	-3.750	6.29	0.015
7.91	0.8	-5.265	3.93	0.008
8.81	0.9	-5.704	3.86	0.008
9.80	1.0	-6.052	3.50	0.009
10.27	1.0	-6.165	3.25	0.009
11.70	1.1	-6.521	2.69	0.014
12.49	1.2	-6.518	2.08	0.004
18.30	3.5	-7.288	0.938	0.002
23.00	14.7	-7.249	0.363	0.001
N(10)	6.7	-6.039	3.20	0.009

<sup>a</sup> In units of  $10^{-14} \text{ W cm}^{-2} \mu\text{m}^{-1}$ .

<sup>b</sup> Statistical uncertainty in units of  $10^{-14} \text{ W cm}^{-2} \mu\text{m}^{-1}$ . Calibrator stars probably introduce  $\pm 5\%$  uncertainty.

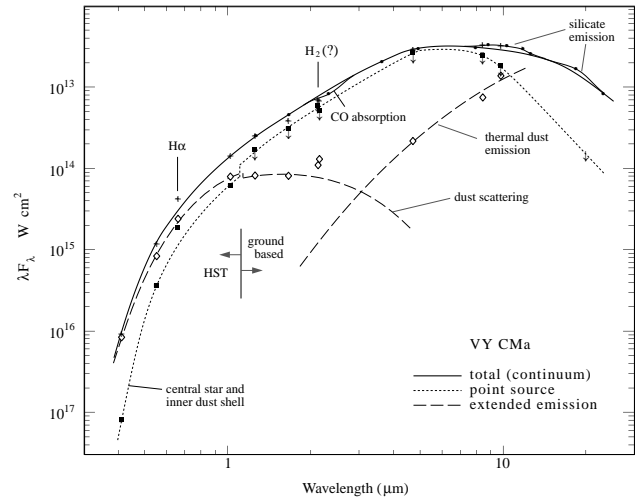


FIG. 7.—Observed optical-to-infrared spectral energy distribution of VY CMA. Filled circles are MLOF photometry with a 9".33 aperture obtained 2000 January 5, plus signs denote the total observed flux in the *HST*/WFPC2 and ground-based IR images at each wavelength. The smooth solid line drawn through these data points represents the total continuum flux of VY CMA. Filled squares indicate the flux of the central star in the optical and near-IR, or the PSF subtracted from the data at mid-IR wavelengths (upper limits of the central source at IR wavelengths, due to limits in spatial resolution). The dotted line drawn through these points indicates the flux of the central object. Unfilled diamonds represent the observed flux from extended emission (total-star). At optical and near-IR wavelengths, the dashed line drawn through these data represents the contribution from scattered light, and at mid-IR wavelengths the dashed line indicates thermal emission from warm dust. The discontinuity in the dashed and dotted lines at 1  $\mu\text{m}$  results from different aperture sizes used to measure the flux of the central star, corresponding to the difference in resolution between *HST* and the ground-based observations.

of some thermal emission by hot grains. Thermal emission by extended circumstellar dust contributes about half of the total flux at  $10\ \mu\text{m}$ , and Forrest, McCarthy, & Houck (1979) find that at  $20\ \mu\text{m}$  more than 90% of the total flux is from extended circumstellar dust.

#### 4. CIRCUMSTELLAR STRUCTURE IN THE IMAGES

Our images cover a wide wavelength range from the standard blue and visual out to  $10\ \mu\text{m}$  and allow us to map the distribution of scattered starlight and warm dust. The optical and near-IR images show similar circumstellar structures, but the thermal-IR images ( $5$  to  $10\ \mu\text{m}$ ) reveal an elongated distribution of dust not seen at shorter wavelengths. We discuss models for VY CMA's circumstellar geometry in § 6, together with its mass-loss history and evolutionary status. Throughout the rest of this paper we adopt the physical parameters summarized in Table 5.

##### 4.1. The Optical and Near-Infrared Images

Our WFPC2 and near-IR images reveal a complex distribution of material around VY CMA, with an obvious lack of spherical symmetry and no clear indication of axisymmetric structures like those seen in the nebulae surrounding many other evolved mass-losing stars. VY CMA's well-known asymmetric nebula is obvious in our WFPC2 images (Figs. 1 and 2), where the brightest nebulosity extends to the south and west of the star. The new images also show a faint outer halo of emission in all directions. The asymmetry is less pronounced at longer wavelengths. The circumstellar nebula includes three or more large reflection arcs, some relatively bright condensations or clumps of dusty knots, several small unresolved knots near the star, and other less prominent filamentary structures. In the following discussion we refer to features labeled in Figure 8, a sketch of the circumstellar nebula.

1. At least three *bright reflection arcs* are conspicuous in the WFPC2 images. Two of these can be seen in the near-IR (Fig. 4) and were discussed by Monnier et al. (1999), but the WFPC2 data greatly alter their interpretation. The most prominent structure is the "curved nebulous tail" or northwest arc, which can be seen visually through a telescope (Herbig 1972; Perrine 1923) and extends from  $2''$  to  $4''$  to the west and northwest of the star (Figs. 1 and 4). In the near-IR data of Monnier et al., this structure appeared to be part of a spiral pattern made by a continuous plume or stream of ejecta (see their Fig. 3). However, as Figures 1 and 2 show, with the higher resolution of WFPC2 the northwest arc turns back toward the star at a radius of about  $4''$  and does not match Monnier et al.'s plume model. It also resembles the two fainter arcs to the south and southwest of the star. Moreover, it does not connect with the southwest condensation as the near-IR images seem to suggest. The other two

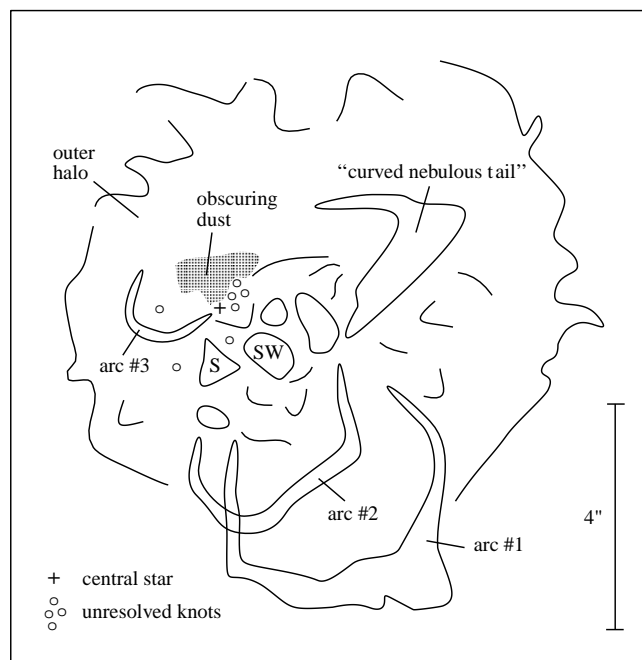


FIG. 8.—Sketch of the various structures seen in the WFPC2 and near-IR images of VY CMA.

arcs, at distances of  $2''$  to  $4''$  and  $5''$  to  $7''$  from the star ("arcs 2 and 1" in Fig. 8, respectively) are best seen in the F547M and F656N filters. Arc 2 is also visible in the near-IR images and was mentioned briefly by Monnier et al. (1999). The geometric width of these arcs is generally no more than  $0''.5$ . Another narrow faint structure, arc 3, is barely visible to the east of the star in the F547M and F656N images. We discuss the nature of these features in § 6.2.

2. Several *bright nebular condensations* are located  $1''$  to  $2''$  south and southwest of the star. The WFPC2 images resolve these into numerous small knots (Figs. 2b and 2c). The two most prominent clumps of knots are labeled "S" and "SW" in Figure 8. Both are visible in all of the WFPC2 images, but their brightness ratio changes with wavelength; feature S is relatively fainter at longer wavelengths. This trend continues into the near-IR so that the S feature is no longer distinguishable at  $2\ \mu\text{m}$  (Fig. 4) though SW is prominent in all four near-IR filters. Monnier et al. (1999) suggested that the IR-bright SW clump is "component B" reported as a moving companion star by early optical observers. Their identification is based on previously measured positions for B. However, at optical wavelengths the S component, which is not clearly visible in the near-IR images, is equally bright or brighter than SW and equally close to the position quoted by Herbig (1972) for B. So it is uncertain whether SW or S is the same as B. We cannot

TABLE 5  
ADOPTED PHYSICAL PARAMETERS FOR VY CMA

Parameter	Value	Comment
Distance .....	1.5 kpc	Herbig (1972); Lada & Reid (1978); Marvel (1997)
Luminosity .....	$5 \times 10^5 L_{\odot}$	
Radius .....	$2 \times 10^8\ \text{km} = 13\ \text{AU}$	Saturn's orbit $r \sim 9.5\ \text{AU}$
Temperature .....	3000 K	From spectral type
Spectral type .....	M5e Ia	Humphreys (1974)
Expansion velocity .....	$35\ \text{km s}^{-1}$	From OH masers (see text)

unambiguously identify any of the optical “companions” with present-day clumps in the WFPC2 images, but it is interesting that we now see two visually bright clumps, S and SW, near where the visual observers reported one. Either the various knots and condensations are changing their structure and positions on time scales of only a few decades, or, as seems equally likely, variable illumination of the clumps might appear as moving companion stars at lower resolution—as in Wallerstein’s (1978) “rotating holey dust cloud” hypothesis.

3. Several *compact knots* with characteristic sizes of the order of  $0''.07$  or 100 AU are located within  $\sim 0''.6$  west of the star (see Fig. 2a). Like most other features mentioned in this paper, these are dusty condensations seen in scattered continuum light; compared with the star, they are not brighter in the F656N ( $H\alpha$ ) filter. In the F410M filter each knot appears roughly 2% to 5% as bright as the central star, but their sizes and distances from the star indicate that they should intercept only about 1% of the total stellar flux. Moreover, their F410M/F547M colors are 2 to 3 mag bluer than the central star. These facts combine to suggest that we see the knots through relatively less line-of-sight local extinction (see also § 3).

4. Many faint, *thin filamentary structures* scattered throughout the nebula give it a disordered appearance in the WFPC2 images. Their F410M/F547M flux ratios are typically more than 2 mag bluer than the central star.

#### 4.1.1. The Large-Scale Asymmetry

The WFPC2 and near-IR images do not show an obvious axis of symmetry, but the combined color image in Figure 3 seems to us to hint that a northeast-southwest axis may exist, with the northeast lobe missing because of extreme faintness or high obscuration. Kastner & Wein-

traub (1998) predicted that an opposing lobe might be found there, based on the wavelength dependence of the central peak’s apparent position that we mentioned in § 3. Some nebulosity extends about  $3''$  to the east in the F547M and F656N images, and the F1042M filter shows a more symmetric distribution of scattered light. No emission is detected to the east of the star in our *J* and *H* images, although the  $2.14\ \mu\text{m}$  image shows emission contours that are nearly concentric about the star.

To investigate the variation of reddening across the nebula, we show the ratios of the fluxes in the images, F410M/F547M and F410M/F1042M, in Figures 9a and 9b. The extended emission east of the star is prominent in Figure 9a, where arc 3 and the knots S and SW are all quite red. These features are most likely highly obscured or possibly contain dust grains with different scattering properties than in other parts of the nebula. Some individual small-scale condensations in arcs 1 and 2 and the central star are also very red. All parts of the nebula are bluer than the central star. Knot SW, the tip of the northwest arc, and part of arc 2 are all highly reddened in Figure 9b. The most striking aspect of Figure 9b, however, is the very red extended emission reaching  $2''$  to  $4''$  to the north and east of the star. This indicates high extinction along the line of sight in this region and may provide a partial explanation for the strong asymmetry.

If the nebula has a northeast-southwest axis of symmetry, then the light we see in the southwest and northeast regions has been scattered through angles predominantly less and more than  $90^\circ$ , respectively. Since backscattering is usually less efficient than forward scattering, this offers an additional reason for the northeast side to be relatively faint. The Homunculus nebula of  $\eta$  Car is a well-known example showing the backscattering/forward-scattering asymmetry

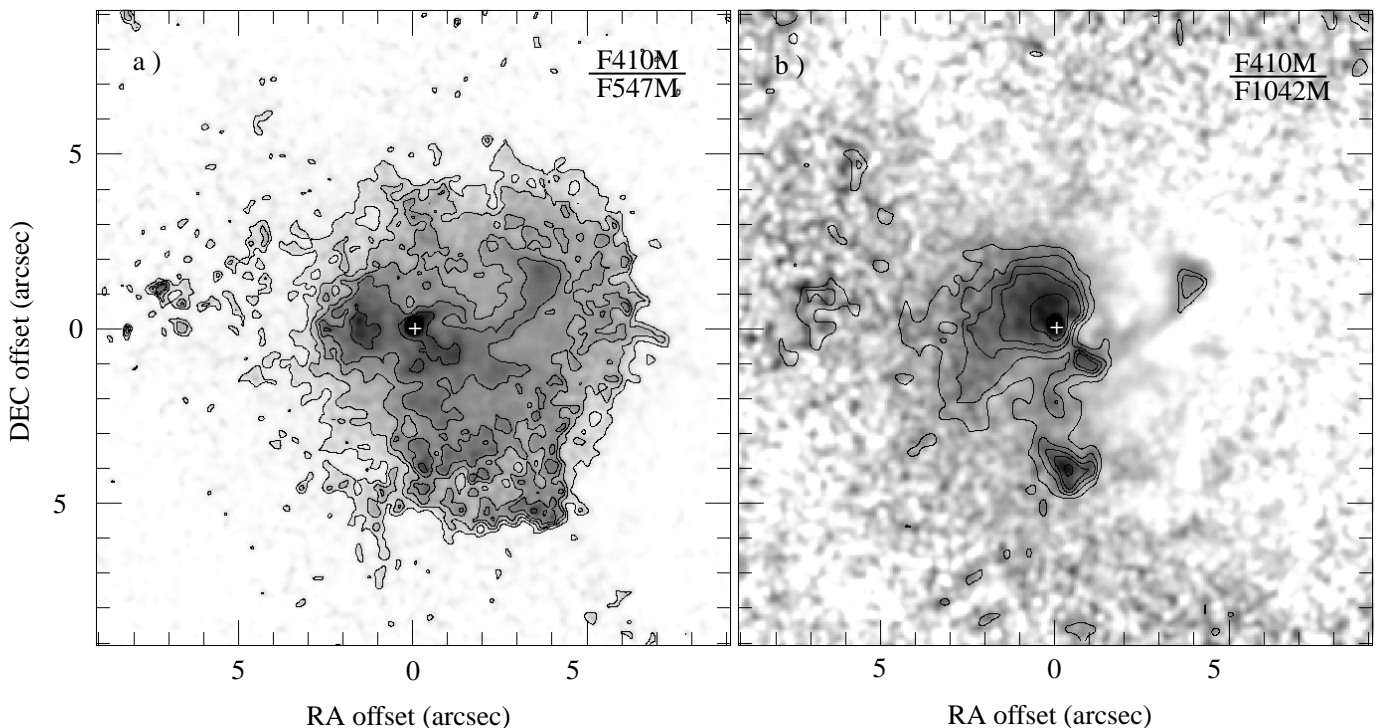


FIG. 9.—Flux ratios of the WFPC2 images. Darker areas indicate relatively red colors. (a) Flux ratio of the F410M and F547M filters, approximating a Strömgen  $v-y$  color index. Contours are smoothed with a 2 pixel Gaussian and drawn at  $v-y = 0.75, 1.31, 1.75, 2.06,$  and  $2.5$  mag. (b) Flux ratio of the F410M and F1042M filters. Contours are smoothed with a 5 pixel Gaussian and drawn at 4.36, 4.72, 5, 5.24, and 5.75 mag.

(Morse et al. 1998). Herbig's (1972) polarization map of VY CMa shows strong polarization southwest of the star but much weaker polarization to the east and northeast; the explanation for this difference very likely involves the scattering angles. In summary, a combination of higher extinction and inefficient backscattering can easily account for the relative lack of visual-wavelength nebulosity northeast of VY CMa, even if the mass distribution is almost symmetric along a northeast-southwest line. Long-integration images, especially at red wavelengths, may reveal a more symmetric nebula (compare Figs. 1b and 1d).

#### 4.2. Mid-IR Imaging

The mid-IR images in Figure 5 represent thermal emission by warm dust and appear different from the near-IR and WFPC2 images. At 4.7, 8.4, and 9.8  $\mu\text{m}$  we see extended structure elongated along an east-west axis, at radii less than 2". The geometric interpretation is not obvious, because it is difficult to distinguish between an equatorial or bipolar distribution of dust. The 4.7  $\mu\text{m}$  peaks are separated by about 1" along a position angle of  $98^\circ$  (or  $278^\circ$ )  $\pm 5^\circ$ , equidistant from the star. At 8.4 and 9.8  $\mu\text{m}$  the separation is larger, about 1.4" and 1.6", respectively. This is qualitatively reasonable since grain temperatures should decrease with distance from the star, but this result is also sensitive to the wavelength dependence of the spatial resolution and should be interpreted with caution. Both the  $F_\lambda(9.8 \mu\text{m})/F_\lambda(4.7 \mu\text{m})$  and the  $F_\lambda(8.4 \mu\text{m})/F_\lambda(4.7 \mu\text{m})$  ratios for the emission from these peaks (measured in a 3" diameter aperture) are consistent with a grain temperature of about 300 K (assuming optically thin emission and a grain emissivity  $Q_{\text{abs}} \propto \lambda^{-1}$ ). The blackbody temperature for grains at 0.5 to 1" (750 to 1500 AU) from a  $5 \times 10^5 L_\odot$  star is about 200 to 270 K. The slight heat excess in the grains of 10% to 30% above the expected blackbody temperature indicates a characteristic grain size between 0.3 and 1  $\mu\text{m}$  (using the emissivities published by Draine & Lee 1984).

Illusory features can be caused by defective PSF subtraction, involving small positional mismatches or variations in atmospheric seeing. In this case, however, the elongated emission has roughly the same orientation at all wavelengths and the derived grain properties are consistent. However, we cannot be certain that the PSF subtraction is not completely free of artifacts, so the elongated structure within 1" to 2" from the star should be regarded as tentative and requires confirmation by future observations.

The 8.4 and 9.8  $\mu\text{m}$  images also show faint emission at 2" to 5" from the star, somewhat more extended toward the east and west. The 9.8  $\mu\text{m}$  outer contours are relatively compressed northeast of the star, suggesting a real asymmetry in the halo. The dust at such distances is too cool to detect in the 4.7  $\mu\text{m}$  image. About 3" (4500 AU) west of the star we measure

$$F_\lambda(8.4 \mu\text{m})/F_\lambda(9.8 \mu\text{m}) \approx 0.5 ,$$

which suggests grain temperatures a little above 150 K. Considering the star's luminosity, such temperatures exceed the blackbody temperatures at 4500 AU from the star by 37%, which would occur with grain sizes of the order of  $a \sim 0.3 \mu\text{m}$ . This estimate for the grain size is consistent with the lower end of that estimated above for grains closer to the star. Of course, there will actually be a distribution of grain sizes in the nebula, but  $a \sim 0.3 \mu\text{m}$  is probably reliable to within an order of magnitude.

In the following discussion, we adopt a very simple two-component model for the dust: (1) the inner elongated emission comes from warm silicate grains with a  $\sim 0.3 \mu\text{m}$ ,  $T \approx 300$  K, located about 750 AU from the star, and (2) cooler grains at distances of 4500 AU or so have a  $\sim 0.3 \mu\text{m}$ ,  $T \approx 150$  K. The required emission optical depths at 9.8  $\mu\text{m}$  are of the order of 0.06 and 0.009 for the warm and cool components, respectively. The optically thick ( $\tau \approx 2$ ) 10  $\mu\text{m}$  emission previously reported (e.g., Le Sidaner & Le Bertre 1996) must come from dust that is closer to the star than the emission resolved here.

#### 5. SURFACE PHOTOMETRY AND MASS LOSS

In this section we use photometry based on the WFPC2 and IR images to estimate the amount of mass in VY CMa's nebula and the implied mass-loss rates.

##### 5.1. Surface Brightness in the WFPC2 Images and the Mass of the Nebula

We can use the surface brightness of scattered light to estimate the amount of circumstellar dust, using a fairly conventional model such as our analysis for IRC+10420 (Humphreys et al. 1997). As a well-defined basis for comparison, we consider a spherically symmetric scattering nebula in which the density of dust is proportional to  $r^{-2}$ , illuminated by a central source. Suppose that each grain scatters light isotropically; the main results quoted below are dominated, in practical cases, by scattering angles around  $90^\circ$ . Let  $I(\theta)$  denote the apparent surface brightness or specific intensity seen at apparent angular distance  $\theta$  from the center (in some particular wavelength interval, of course), while  $F$  is the corresponding total apparent flux from the entire object, i.e.,  $F = \int I d\Omega$ . The ratio  $I(\theta)/F$  is not affected by interstellar extinction. If  $r$  is the projected linear radius for a given value of  $\theta$ , then let  $\tau_{\text{sc}}(\theta)$  denote the optical thickness for scattering only, along a radial path outward from radius  $r$ . With an  $r^{-2}$  density distribution,  $\tau_{\text{sc}}$  is inversely proportional to  $\theta$  and the optical thickness for scattering along our line of sight through the spherical nebula is  $\pi\tau_{\text{sc}}(\theta)$ . Under these conditions,  $\tau_{\text{sc}}(\theta)$  is indicated by a particular observable dimensionless quantity,

$$\frac{\theta^2 I(\theta)}{F} \approx \frac{\tau_{\text{sc}}}{8} \exp(-\eta\tau_{\text{sc}}) ,$$

for  $\tau_{\text{sc}}$  less than about 1. Here the exponential factor is merely a convenient approximation based on numerical simulations, with  $\eta \approx 0.85$  for the pure scattering case and  $\eta \approx 1.25$  for a grain albedo (reflectivity) of 0.5. The reflectivity dependence is sufficiently weak, as a practical matter, that we can safely adopt an albedo of 0.5, at least for blue to red wavelengths. For clarity we emphasize that  $F$  is the observable emergent flux, not the flux that would be seen in the absence of circumstellar dust. Moreover, the value of  $\theta^2 I(\theta)$  does not depend on which units one uses to measure  $\theta$ . In the outer parts of the nebula we find the familiar law for reflection nebulae:  $I(\theta) \propto \theta^{-3}$ .

For VY CMa the defects of a spherical model are obvious. Nevertheless, as an average over all radial directions, the formula quoted above appears to have a rough validity as we explain below; while a substantially improved model would require information that is not available, concerning the three-dimensional distribution of dust as well as nonisotropic scattering and other grain properties.

Figures 10a and 10b show the observed parameter  $\theta^2 I(\theta)/F$  averaged over many pixels in the F547M and F1042M WFPC2 images of VY CMA. (The F410M and F656N images have lower signal-to-noise ratios.) In each figure the solid curve represents an average over all position angles except near the diffraction spikes. The other two curves represent sectors roughly aligned with the suspected major axis of the configuration: northeast (position angles  $30^\circ$ – $60^\circ$ ) and southwest (position angles  $210^\circ$ – $240^\circ$ ). The sampling width is  $\Delta\theta \approx 0''.14$ . Aside from peaks representing obvious local structures, each curve follows the  $I(\theta) \sim \theta^{-3}$  law reasonably well in the  $\theta$  range from  $1''.4$  to  $6''$ . Deviations from the trend are typically less than a factor of 2, compared with a factor of the order of 100 for the relevant radial variation of surface brightness. The central object's diffraction pattern is too weak to affect Figure 10 significantly, especially for  $\theta > 2''$ ; see Figure 8 in Humphreys et al. (1997). The sharp decline beyond  $7''$  in the southwest direction occurs at the outer edge of arc 1. Similar distributions along the perpendicular axis, northwest and southeast, are intermediate between the SW and NE samples in Figure 10. Thus we conclude that the average density of dust is roughly proportional to  $r^{-2}$  at distances 2000 to 9000 AU from the star (ages  $\sim 200$  to 2000 yr?). This is not surprising and need not imply a steady outflow; an inverse-square distribution can result from a succession of several or many ejection events, especially if each produces a range of outward velocities.

Quantitatively, at an example radius  $\theta = 3''$  we find  $\theta^2 I(\theta)/F \approx 0.03$  and 0.015 in the F547M and F1042M images; which imply  $\tau_{sc} \approx 0.4$  and 0.14, respectively, at  $r \approx 4500$  AU (multiply these values by about 2 to get the total optical depth including absorption). The ratio between the two values is consistent with the wavelength dependence expected for grains moderately larger than “normal.” It is possible that  $I(\theta)$  deviates at small radii from the  $\theta^{-3}$  trend merely because the dust is so thick there that our formula becomes inapplicable. With conventional grain parameters and a gas-to-dust mass ratio of  $\sim 100$  (Savage & Mathis 1979), these results indicate an ejecta mass of roughly  $0.2 M_\odot$  between radii of 2000 and 9000 AU. Corrections for the suspected northeast-southwest extinction gradient are too

uncertain to attempt at present, but would most likely increase the mass. An estimate using the same method for scattered light at  $2 \mu\text{m}$  is consistent but depends more strongly on grain size. The implied mass-loss rate is consistent with estimates based on other methods, and is discussed in § 5.3.

The masses of large individual structures in the nebula are potentially significant, especially if each represents a separate major outburst. Surface brightnesses give limited but useful information on the northwest arc, for example. We use the same notation as above, except that here  $I_{loc}$  denotes a *local* specific intensity observed on a resolved structure at angular distance  $\theta$  from the star. Calculations show that generally, with the assumptions employed above,  $\theta^2 I_{loc}/F$  cannot exceed about 0.1, even if absorption is weak and the observed density enhancement has an optimum scattering thickness. For geometric reasons, efficient forward scattering does not alter this statement. However, a well-resolved part of the northwest arc appears to violate the brightness limit at visual wavelengths. There, within an area of roughly 2 arcsec<sup>2</sup> located about  $3''.2$  from the star, we find  $\theta^2 I_{loc}/F \approx 0.2$  in the F547M image. The simplest explanation has two parts. First, very likely the northwest arc is located favorably in the patchy nebula, with unusually small extinction between the star and the arc. In that case the observed large-scale emergent flux  $F$  becomes inappropriate as the reference value in our formula. Second, the optical depth in the northwest arc is probably close to optimal, of order unity at visual wavelengths; smaller values would give less reflection but larger values would entail more absorption. This idea is supported by the fact that the outer tip of the northwest arc, about  $5''$  from the star, becomes relatively more prominent toward longer wavelengths. If the visual-wavelength optical thickness is unity and the projected area is 2 arcsec<sup>2</sup>, then the usual assumptions about the gas-to-dust ratio, etc., lead to an order-of-magnitude mass estimate of  $2 \times 10^{-3} M_\odot$ . Since this represents only the brightest part of the northwest arc, let us adopt  $3 \times 10^{-3} M_\odot$  as the total mass of the structure—perhaps a percent of the mass of the visible nebula.

Figure 10a shows evidence for mass loss at a reduced rate more than 1000 yr ago, especially southwest of the star. The

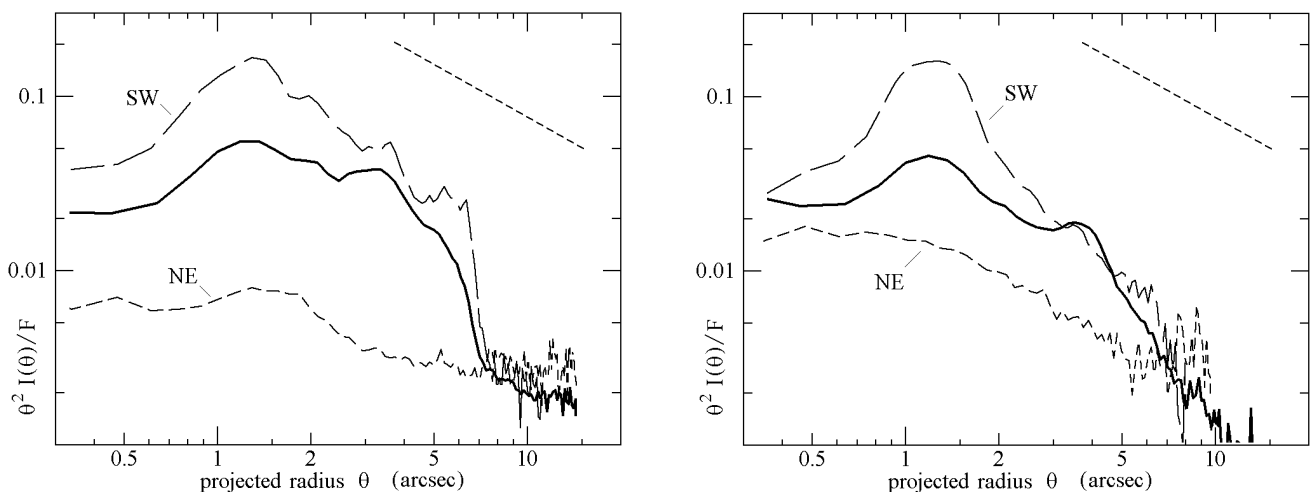


FIG. 10.—Observed dimensionless quantity  $\theta^2 I(\theta)/F$  averaged over broad ranges of position angles in the WFPC2 data, for the F547M (a) and F1042M (b) filters. As explained in the text, this quantity indicates average optical depth for scattering by grains as a function of radial distance from the star. The solid curve shows an average over practically all position angles, while “SW” and “NE” refer to limited sectors. The dashed line in the upper right corner shows the slope for  $I \propto \theta^{-3}$ , characteristic of an idealized reflection nebula with density proportional to  $r^{-2}$ .

average surface brightness at locations in the range  $7'' < \theta < 11''$  appears to be real and is consistent with an  $I(\theta) \sim \theta^{-3}$  dependence. Its brightness is roughly one-fourth the value that would have been expected from an extrapolation of the densities seen at smaller radii.

### 5.2. Infrared Estimates of the Circumstellar Mass

The mid-IR images in Figure 5 show thermal emission from extended circumstellar dust located roughly  $0.5''$  to  $5''$  (750 to 7500 AU) from the central star. This can be used to estimate the mass of this circumstellar material, with a few assumptions about the dust properties. The mass of the emitting grains is given by

$$M_{\text{dust}} = \frac{4D^2 \rho \lambda F_\lambda}{3(\lambda Q_\lambda/a) B_\lambda(T)},$$

where  $D \approx 1.5$  kpc is the distance to VY CMa;  $F_\lambda$  is the observed mid-IR flux;  $a \approx 0.3 \mu\text{m}$  is grain radius;  $\rho \approx 3 \text{ g cm}^{-3}$  is mass density in a grain;  $Q_\lambda$  is a grain's efficiency for emission and absorption of radiation, and  $B_\lambda$  is the Planck specific intensity at temperature  $T$ . According to Draine & Lee (1984), the quantity  $\lambda Q_\lambda/a$  at  $\lambda = 9.8 \mu\text{m}$  is roughly 10 for silicate grains and is nearly independent of grain size. In the  $9.8 \mu\text{m}$  image in Figure 5, the two bright peaks with  $T \approx 300$  K contribute roughly half of the total flux while the extended dust with  $T \approx 150$  K produces most of the remainder; so each component has  $\lambda F_\lambda \approx 7.2 \times 10^{-14} \text{ W cm}^{-2}$ . Thus we find about  $10^{-4} M_\odot$  and  $4 \times 10^{-3} M_\odot$  of dust in the warm and cool components, respectively. A normal gas-to-dust ratio of 100 then implies a total nebular mass of roughly  $0.4 M_\odot$  within 7500 AU of the star. As usual this estimate may easily be in error by a factor of 2 or conceivably more. A substantial mass of cooler material at large radii may have been omitted here.

### 5.3. The Mass-Loss Rate

We have determined two mutually independent estimates of the nebular mass around VY CMa:  $0.2 M_\odot$  or perhaps somewhat more at radii between 2000 and 9000 AU, based on the visual wavelength reflection nebula, and  $0.4 M_\odot$  at radii less than 7500 AU based on mid-IR thermal emission. As a compromise, we adopt  $0.4 M_\odot$  at all radii out to 9000 AU. Lacking any other velocity indicator, we assume that the maser velocity of  $35 \text{ km s}^{-1}$  is also the expansion speed. Then 9000 AU corresponds to an age of 1200 yr, and we find a mass-loss rate of roughly  $3 \times 10^{-4} M_\odot \text{ yr}^{-1}$  averaged over that time. This is consistent with earlier estimates (Danchi et al. 1994), though many sources of uncertainty are obviously possible for our results and previous work. It is near the maximum possible for single scattering in a wind driven by radiation pressure on dust for a star of VY CMa's luminosity.

The unresolved central source of thermal IR emission gives a separate estimate of the *current*, or at least recent, mass-loss rate. Emission within  $0.5''$  or 750 AU comes from the warmest dust, in material ejected during the past 100 yr or so. If the relevant grain temperatures are between 500 and 1000 K, then the observed  $9.8 \mu\text{m}$  flux of  $1.88 \times 10^{-14} \text{ W cm}^{-2} \mu\text{m}^{-1}$  implies an unresolved circumstellar mass of roughly  $10^{-2}$  to  $10^{-3} M_\odot$ . The corresponding mass-loss rate is of the order of  $10^{-5}$  or  $10^{-4} M_\odot \text{ yr}^{-1}$ , interestingly smaller than the longer term average rate noted above. However, this may be an underestimate if the dust close to the star is optically thick enough at  $9.8 \mu\text{m}$ . In that case, the

mass distribution must be quite patchy or disklike, since it allows visible light to escape from that region into the reflection nebula.

As noted in § 5.1, the average density decreases faster than  $r^{-2}$  at radii around 9000 AU, though some material exists farther out. This fairly definite outer radius probably indicates that VY CMa has been in a state with enhanced mass loss during the past millennium, or perhaps only the past few centuries if our assumed  $35 \text{ km s}^{-1}$  velocity is an underestimate.

## 6. THE CIRCUMSTELLAR ENVIRONMENT, MASS-LOSS HISTORY, AND EVOLUTIONARY STATUS

Given the complex structure and apparent lack of any kind of symmetry in the optical and near-IR images of VY CMa's nebula, deducing the geometry of the circumstellar environment is not a straightforward task. Bipolar outflows seem almost ubiquitous in nebulae surrounding evolved stars, and a disklike geometry has also been invoked by several authors to explain various observations of VY CMa. We consider the merits of both these axisymmetric geometries regarding the morphology seen in the images presented here. We also consider the possibility that many of the observed features, especially the arcs and condensations, may be explained by a nonaxisymmetric geometry involving localized, episodic mass loss from the star.

### 6.1. Geometry of the Circumstellar Envelope

VY CMa's nebula is obviously not spherical, and the optical and near-IR images do not show any obvious axial symmetry, such as a bipolar outflow or circumstellar disk. If there is a bipolar outflow, one of the lobes must be highly obscured or not illuminated at optical and near-IR wavelengths. The elongated mid-IR emission in Figure 5 could be interpreted as evidence for bipolarity. However, in such a model it is not clear how the nearly east-west axis can be reconciled with the structures observed at shorter wavelengths.

Previous studies favor a predominantly equatorial distribution of material around VY CMa. Herbig (1970) concluded that a thick ring or disk was needed to explain the observed infrared energy distribution, invoking a flared disk or ring in latitudes  $10^\circ$  to  $30^\circ$ . The outer region of the disk responsible for the mid-IR emission had a temperature of 350 K and was located a few arcseconds from the star. This is consistent with the warm dust component we derived from the elongated mid-IR emission in Figure 5. The hot dust in the inner region of the disk in Herbig's model would not be spatially resolved by our mid-IR observations and could be responsible for most of the long-wavelength emission from the central point source. Furthermore, Herbig's model predicted that the hypothesized disk would be seen at high inclination and would obscure the central star, so that only  $\sim 15\%$  of the observed optical flux would come directly from the central source. This is in good agreement with our photometry of the central source in Figure 7 (see also § 3), which may include some light scattered by circumstellar dust close to the star. Thus, our observations support Herbig's interpretation of the infrared energy distribution that VY CMa is surrounded by a nearly edge-on equatorial ring or disk of dust.

Maser observations of VY CMa have also been interpreted as evidence for an expanding equatorial disk seen at an oblique angle (van Blerkom & Auer 1976; Rosen et al.

1978; Benson & Mutel 1979, 1982; Morris & Bowers 1980; Bowers et al. 1983; Deguchi et al. 1983; Richards et al. 1998). The distribution of maser spots is elongated along a predominantly northeast-southwest axis, with the blue-shifted masers concentrated toward the northeast. The path lengths required for maser amplification can be achieved in the near and far sides of an expanding disk, with the near side of the disk toward the northeast of the star at a position angle of  $\approx 50^\circ$  (Bowers et al. 1983). The northeast-southwest axis then represents the polar/rotation axis of the star and disk, which is tilted by  $15^\circ$  to  $30^\circ$  to our line of sight (Morris & Bowers 1980). In our discussion of the images (see § 4), we described the slightly flattened distribution of thermal emission from dust (Figs. 5b and 5c) that extends out to  $5''$  from the star. The mid-IR contours show obvious foreshortening to the northeast, suggesting that this flattened distribution is tilted with an axis of symmetry at a position angle of  $\sim 30^\circ$  to  $40^\circ$ , consistent with the maser observations.

Thus, the most likely geometry for VY CMA's nebula, consistent with the WFPC2 and IR images and previous observations, is an equatorial disk with a more or less bipolar axis projected roughly northeast-southwest, and with the southwest lobe closer to us. Monnier et al. (1999) favor a similar geometry based on high-resolution near-IR imaging. High extinction to the east and northeast of the star, together with backscattering by dust on the far side of the nebula, is probably responsible for the apparent asymmetry in optical images (see § 4.1.1). An axially symmetric model with most of the mass confined to low latitudes can explain several observational properties of VY CMA's nebula, but does not account for prominent structures in the *HST* and near-IR images; the bright reflection arcs and condensations distributed asymmetrically about the star.

### 6.2. Evidence for Localized Ejections

The filaments, arclike structures, and bright clumps are evidence for multiple, asymmetric mass-loss events. Each arcsecond from the star translates to an age of about 200 yr, for  $35 \text{ km s}^{-1}$  expansion in the plane of the sky and a distance of 1.5 kpc. The ejection times then range from about 1000 yr ago for arc 1 to as recent as only 200 yr ago for the south and southwest clumps. In § 5 we showed that the average mass-loss rate has been on the order of  $4 \times 10^{-4} M_\odot \text{ yr}^{-1}$  for the past 1000 yr, with evidence that it was somewhat lower before that. Thus, these structures appear to be part of the same enhanced mass-loss episode that began about 1000 yr ago. These estimates do not consider motion out of the plane of the sky and expansion velocities much different than  $35 \text{ km s}^{-1}$ . Depending on their ejection velocities, these features could be the result of multiple events or one single mass-loss episode.

The arcs are potential clues to the behavior of the central star. These structures do not have the appearance of continuous outflow streams, and one would not expect multiple plumes from the star to preserve their approximate directions in space for hundreds of years. Thus, *each arc was most likely produced by an ejection event localized on the stellar surface, not by long-term mass loss.* The idea of localized outbursts is a good working hypothesis because it is very compatible with the morphology of the arcs (they qualitatively resemble solar ejecta) while the physical nature of VY CMA seems well-suited to sporadic ejections with random directions (see below). The data quantitatively exclude some possible acceleration mechanisms. For example, the arcs are

too massive to have been ejected by radiation pressure acting on dust. As noted in § 5.1, the mass of the northwest arc appears to be roughly  $3 \times 10^{-3} M_\odot$ . It covers no more than 0.5 sr of solid angle relative to the star. With these quantities and the star's luminosity, we calculate that radiation pressure cannot give the material enough momentum unless the ejection process extends over several hundred years. Preserving directionality so long is implausible, and relatively narrow parts of each arc seem incompatible with such a long timescale for the ejection event. Radiation pressure has probably caused appreciable acceleration since the material left the star, but the initial ejection must have been induced by other processes.

The dynamical timescale of VY CMA's envelope is roughly 3 yr. The basic timescale for either a nonradial dynamical instability or a magnetic/convective event (analogous to solar activity) is likely to be of the same order of magnitude, or perhaps moderately longer. If so, then a temporary mass-loss rate of the order of  $10^{-3} M_\odot \text{ yr}^{-1}$  could have produced the northwest arc. This is only several times larger than the average rate (§ 5.3 above). The northwest arc has a kinetic energy of the order of  $3 \times 10^{43}$  ergs at a velocity of  $35 \text{ km s}^{-1}$ , or about 10 times larger, of course, if the speed is  $100 \text{ km s}^{-1}$ . Such energies are modest in the sense that VY CMA radiates  $10^{44}$  ergs in less than a day. On the other hand, the same amount of energy is very roughly comparable to the thermal energy present in the outer  $3 \times 10^{-3} M_\odot$  of the star, i.e., in the ejected mass. The apparently random orientations of the ejected arcs suggest that they were produced by relatively localized processes, not strongly aligned with the star's axis or equator. As hinted above, we suspect that these events were magnetic and convective in nature, like solar activity. This conjecture is motivated by the nature of the star as well as by the appearances of the arcs. Large, bright, and variable starspots with accompanying outflow occur on the surface of  $\alpha$  Ori (Gilliland & Dupree 1996; Kluckers et al. 1997; Uitenbroek, Dupree, & Gilliland 1998; see also Buscher et al. 1990; Wilson et al. 1992). This makes sense in a red supergiant with its strong convective turbulence and may be commonplace on other red supergiants (Tuthill, Haniff, & Baldwin 1997). Since the outer convective cells in a cool supergiant are comparable in size to the stellar radius (Schwarzschild 1975), the sizes of the VY CMA arcs also seem reasonable in this context. They may be expanding loops or bubbles, caused by localized activity on the star's ill-defined "surface" and analogous to solar prominences that have become disconnected. Of course this suggestion is highly conjectural, but it appears plausible in most respects, the energy budget seems promising, and we are not aware of any obvious major objections to this idea. Nonradial pulsational instability may offer an alternative ejection mechanism, but the distinction between this and a convective/magnetic scenario may be blurred in an extreme red supergiant like VY CMA, with large convective cells. Perhaps the bright clumps of small knots were also produced by activity on the star's surface.

### 6.3. Comments on VY CMA's Evolutionary State

VY CMA is a very luminous red supergiant with powerful maser emission. It is one of about 10 known M-type supergiants with bolometric luminosities above  $-9.0$  mag. About half of these stars in our galaxy are known OH/IR stars with strong maser emission and high mass-loss rates.

We do not know whether this is a short stage that all of the most massive red supergiants pass through as they shed their outer layers or whether there is some special condition that leads to the high mass loss and the formation of a dusty disk.

In previous papers (Jones et al. 1993; Humphreys et al. 1997) we have demonstrated that the warm OH/IR supergiant IRC + 10420 is a post-red supergiant shedding its circumstellar dust and suggested that VY CMa is a good candidate for its progenitor red supergiant stage. Other authors have also expressed suspicion that VY CMa might be a precursor of an object like IRC + 10420 (e.g., Wittkowski et al. 1998; Kastner & Weintraub 1995). Several of the different features in VY CMa's circumstellar environment such as the compact knots are also observed close to the central star in IRC + 10420. The bright arcs closely resemble the scalloped shell-like structures we see in the outer parts of IRC + 10420's ejecta (Humphreys et al. 1997). Both stars have obviously undergone multiple, perhaps localized, ejections. However, our present observations do not allow us to tell whether VY CMa is a red supergiant beginning to expel its optically thick dusty envelope, or if it is in the process of creating a thick cocoon like the optically obscured carbon and M stars near the top of the AGB.

VY CMa probably has a large-scale flattened distribution of circumstellar dust in its equatorial plane, and it may also have an axis of rotational symmetry. The presence of an axis of symmetry in a star as large as VY CMa raises important questions about the origin of its flattened disklike structure and possible bipolar lobes. Its flattened halo indirectly suggests that the embedded star itself may not be spherical. However, as a massive star moves redward on the HR diagram, its rotation will slow and any high rotation and flattening in the equatorial region or presence of a disklike structure such as in B[e] stars will be minimized. An obvious solution is to suggest that VY CMa may have originally been a binary and the lower mass companion is now moving through its very extended envelope; perturbing it in such a way as to produce a disk. Red supergiants in binaries are well known and easily recognized by their composite spectra, such as the VV Cephei stars (Cowley 1969); some are well known for atmospheric eclipses, such as VV Cep itself, and  $\zeta$  Aur. In all cases the companion is much hotter, usually a main-sequence B-type star. If VY CMa had such a companion moving through its outer atmosphere, it should have been detected in its spectrum. There is no evidence for a hot companion or atmospheric eclipses in VY CMa's spectroscopic history. We

would therefore have to propose a much lower mass companion that would not be observable.

We have suggested that the arcs in VY CMa's circumstellar nebula may be due to localized ejections, perhaps associated with magnetic and convective disturbances like starspots in its atmosphere. Magnetic fields might also help explain the apparent axisymmetry discussed in § 6.1. A strong magnetic field combined with turbulence will increase the effective viscosity in the star's envelope and will help to transfer angular momentum from the star's interior to the outer layers. This may give rise to a rotational axis of symmetry in the star. Although this comment is speculative, Zeeman splitting of OH emission lines from the very similar red supergiant VX Sgr (Chapman & Cohen 1986) has led to suggestions of a dipole magnetic field model for the asymmetry in its circumstellar envelope (Triglio, Umana, & Cohen 1998). A magnetic field on the order of 1 gauss would provide magnetic pressure comparable to the energy density of VY CMa's wind. If a large-scale dipole magnetic field is present, it may supply an additional mechanism for the desired axisymmetry by focusing the cool wind toward the equator; Matt et al. (2000) present computations of disk structure for AGB winds with  $\sim 1$  gauss magnetic fields. Alternatively, Hege & Langer (1998) conclude that significant spin up can occur in evolved red supergiants leaving the Hayashi limit.

Our multiwavelength images have raised several interesting questions and problems about VY CMa and other very massive evolved stars. Some specific questions can be addressed with future observations. Spatially resolved longslit spectroscopy of the various features in the ejecta would indicate their expansion velocities. At a distance of only 1.5 kpc, additional imaging in the next few years would let us measure the proper motions of the different structures in the ejecta which, when combined with their velocities, would help determine their age and orientation with respect to the central star. And finally, high-resolution polarimetry of the ejecta would resolve the star's axis of symmetry.

Support was provided by NASA through grant GO-7304 from the Space Telescope Science Institute, which is operated by the Association of Universities for Research in Astronomy, Inc., under NASA contract NAS 5-26555. R. D. G. was supported by the NSF and NASA. We are pleased to acknowledge interesting conversations with George Wallerstein, Jon Bjorkman, and John Monnier. We also thank G. F. Lawrence, C. E. Woodward, and J. Song for assistance with the MLOF observations.

#### REFERENCES

- Benson, J. M., & Mutel, R. L. 1979, *ApJ*, 233, 119  
 ———. 1982, *ApJ*, 253, 199  
 Bowers, P. F., Johnston, K. J., & Spencer, J. H. 1983, *ApJ*, 274, 733  
 Buscher, D. F., Baldwin, J. E., Warner, P. J., & Haniff, C. A. 1990, *MNRAS*, 245, 7P  
 Chapman, J. M., & Cohen, R. J. 1986, *MNRAS*, 220, 513  
 Cowley, A. P. 1969, *PASP*, 81, 297  
 Danchi, W. C., Bester, M., Degiacomi, C. G., Greenhill, L. J., & Townes, C. H. 1994, *AJ*, 107, 1469  
 Deguchi, S., Good, J., Fan, Y., Mao, X., Wang, D., & Ukita, N. 1983, *ApJ*, 264, L65  
 de Jager, C. 1998, *A&A Rev.*, 8, 145  
 Draine, B. T., & Lee, H. M. 1984, *ApJ*, 285, 89  
 Eliasson, B., & Bartlett, J. F. 1969, *ApJ*, 155, L79  
 Forbes, F. F. 1971, *ApJ*, 165, L83  
 Forrest, W. J., McCarthy, J. F., & Houck, J. R. 1979, *ApJ*, 233, 611  
 Gehrz, R. D., Smith, N., Low, F. J., Krautter, J., Nollenberg, J., & Jones, T. J. 1999, *ApJ*, 512, L55  
 Gehrz, R. D., & Ney, E. P. 1992, *Icarus*, 100, 162  
 Gehrz, R. D., & Ney, E. P., & Strecker, D. W. 1970, *ApJ*, 161, L219  
 Gillett, F. C., Stein, W. A., & Solomon, P. M. 1970, *ApJ*, 160, L173  
 Gilliland, R. L., & Dupree, A. K. 1996, *ApJ*, 463, L29  
 Hashimoto, J., Maihara, T., Okuda, H., & Sato, S. 1970, *PASJ*, 22, 335  
 Hege, A., & Langer, N. 1998, *A&A*, 334, 210  
 Herbig, G. H. 1970, *ApJ*, 162, 557  
 ———. 1972, *ApJ*, 172, 375  
 Humphreys, R. M. 1974, *ApJ*, 188, 75  
 Humphreys, R. M., & Davidson, K. 1994, *PASP*, 106, 1025  
 Humphreys, R. M., Strecker, D. W., & Ney, E. P. 1972, *ApJ*, 172, 75  
 Humphreys, R. M., et al. 1997, *AJ*, 114, 2778  
 Hyland, A. R., Becklin, E. E., Neugebauer, G., & Wallerstein, G. 1969, *ApJ*, 158, 619  
 Jones, T. J., et al. 1993, *ApJ*, 411, 323  
 Kastner, J. H., & Weintraub, D. A. 1995, *ApJ*, 452, 833  
 ———. 1998, *AJ*, 115, 1592  
 Kluckers, V. A., Edmunds, M. G., Morris, R. H., & Wooder, N. 1997, *MNRAS*, 284, 711  
 Lada, C. J., & Reid, M. J. 1978, *ApJ*, 219, 95

- Le Sidaner, P., & Le Bertre, T. 1996, *A&A*, 314, 896  
Low, F. J., Johnson, H. L., Kleinmann, D. E., Latham, A. S., & Geisel, S. L. 1970, *ApJ*, 160, 531  
Marvel, K. B. 1997, *PASP*, 109, 1286  
Matt, S., Balick, B., Winglee, R., & Goodson, A. 2000, *ApJ*, 545, 965  
McCarthy, D. W. 1979, in *IAU Colloq. 50, High Angular Resolution Stellar Interferometry*, ed. J. Davis & W. J. Tango (Sydney: Univ. Sydney Press)  
Monnier, J. D., Geballe, T. R., & Danchi, W. C. 1998, *ApJ*, 502, 833  
Monnier, J. D., Tuthill, P. G., Lopez, B., Cruzalebes, P., Danchi, W. C., & Haniff, C. A. 1999, *ApJ*, 512, 351  
Morris, M., & Bowers, P. F. 1980, *AJ*, 85, 724  
Morse, J. A., Davidson, K., Bally, J., Ebbets, D., Balick, B., & Frank, A. 1998, *AJ*, 116, 2443  
Ney, E. P. 1974, *ApJ*, 189, L141  
Perrine, C. D. 1923, *PASP*, 35, 229  
Richards, A. M. S., Yates, J. A., & Cohen, R. J. 1998, *MNRAS*, 299, 319  
Rosen, B. R., Moran, J. M., Reid, M. J., Walker, R. C., Burke, B. F., Johnston, K. J., & Spencer, J. H. 1978, *ApJ*, 222, 132  
Rowan-Robinson, M., Lock, T. D., Walker, D. W., & Harris, S. 1986, *MNRAS*, 222, 273  
Savage, B. D., & Mathis, J. S. 1979, *ARA&A*, 17, 73  
Schwarzschild, M. 1975, *ApJ*, 195, 137  
See, T. J. J. 1897, *AJ*, 18, 181  
Serkowski, K. 1969a, *ApJ*, 156, L139  
———. 1969b, *ApJ*, 158, L107  
Smith, N., Gehrz, R. D., & Krautter, J. 1998, *AJ*, 116, 1332  
Snyder, L. E., & Buhl, D. 1975, *ApJ*, 197, 329  
Triglio, C., Umama, G., & Cohen, R. J. 1998, *MNRAS*, 297, 497  
Tuthill, P. G., Haniff, C. A., & Baldwin, J. E. 1997, *MNRAS*, 285, 529  
Uitenbroek, H., Dupree, A. K., & Gilliland, R. L. 1998, *AJ*, 116, 2501  
van Blerkom, D., & Auer, L. 1976, *ApJ*, 204, 775  
van den Bos, W. H. 1927, *BAN*, 3, 263  
Wallerstein, G. 1958, *PASP*, 70, 479  
———. 1978, *Observatory*, 98, 224  
Wilson, W. J., & Barrett, A. H. 1968, *Science*, 161, 778  
Wilson, R. W., Baldwin, J. E., Buscher, D. F., & Warner, P. J. 1992, *MNRAS*, 257, 369  
Wittkowski, M., Langer, N., & Weigelt, G. 1998, *A&A*, 340, L39  
Worley, C. E. 1972, *ApJ*, 175, L93  
Zheng, X. W., Scalise, E., Jr., & Han, F. 1998, *ApJ*, 507, 384